

Title:

Towards an integrated observation and modeling system in the New York
Bight using variational methods, Part II: Representer-based observing
system design

Authors: Weifeng G. Zhang^{a,1}, John L. Wilkin^a and Julia C. Levin^a

^a Institute of Marine and Coastal Sciences, Rutgers, The State University of New Jersey

71 Dudley Road, New Brunswick, New Jersey, 08901, USA

Emails: wzhang@whoi.edu, wilkin@marine.rutgers.edu, julia@marine.rutgers.edu

Corresponding Author:

Weifeng G. Zhang

Tel.: +1 (508) 289 2521

Fax: +1 (508) 457 2194

Email: wzhang@whoi.edu

¹ *Present address:* Woods Hole Oceanographic Institution, Bigelow 410, MS#09, Woods Hole, Massachusetts, 02543, USA

Abstract

As part of an effort to build an integrated observation and modeling system for the New York Bight, this study explores observing system design using a representer-based method. The Representer of a single observation describes the covariance between the observed quantity and ocean state at all locations at any time. It is related closely to the influence of the observation on control variable correction in a 4D Variational data assimilation system. We prove that these properties hold for the combination of representers that is associated with an arithmetic function of model variables or a group of observations. The representer-based method is used here to identify which of a set of proposed tracks for an autonomous coastal glider is better for predicting horizontal salt flux within the Hudson Shelf Valley in a 2-day forecast period. Twin experiments confirm the result. The system is also used to compare different observation strategies. We show that a glider that traverses a regular transect influences a larger area than a continuously profiling mooring, but the mooring carries stronger influence at the observation location. The representer analysis shows how the information provided by observations extends toward the dynamically upstream and how increasing the duration of the analysis window captures more dynamical connections and expands the area of influence of the observations in data assimilation. Overall, the study demonstrates that the representer methodology can quantitatively contrast different observational strategies and determine spatial patterns and temporal extent of the influence of observations, both of which are helpful for evaluating the design of observation networks.

Keywords: representer; adjoint; observing system design; adaptive sampling; observation influence; New York Bight

1. Introduction

Ocean observation technologies developed in recent decades have significantly expanded the scope and density of data available for coastal oceanic research. While largely used to study the oceans directly, observations are also increasingly used to correct numerical models using methods of data assimilation developed to improve state estimation and ocean prediction. The capability to simultaneously deploy numerous instruments of differing types during intensive observing experiments, and the development of sustained integrated coastal ocean observing systems, has bolstered the demand for objective methods of evaluating observational strategies. Observing system design considerations are generally motivated by a need for targeted observation of a particular aspect of regional ocean circulation, or a desire to deploy instruments in an adaptive sampling mode to capture transient or moving features.

Designing a targeted observation program in conjunction with a data assimilation system has the objective of selecting the most efficient observation types and locations to improve model analysis or forecast of a certain aspect of interest given known instrument capabilities and practical logistical constraints on their deployment and operation.

Targeted observation design is an active research topic in the numerical weather forecast community (Langland, 2005; Rabier et al., 2008). Berliner et al. (1999) used mathematical terms to summarize differing design approaches. These are Singular Vector-type techniques (Leutbecher, 2003; Palmer et al., 1998), Adjoint Sensitivity-type techniques (Bergot, 1999; Wu et al., 2007), Observation Sensitivity-type techniques (Baker and Daley, 2000; Langland and Baker, 2004), and Ensemble Transform-type techniques (Bishop and Toth, 1999; Bishop et al., 2001).

Singular Vector techniques find the most rapidly growing error structures associated with a norm over a finite time interval. The norm is chosen to describe an aspect of interest, e.g. forecast uncertainty or total energy. The design rationale is that in order to capture the chosen aspect of ocean circulation in the data assimilation (DA) system, the fastest-growing singular vector error structures in the model ought to be constrained by observations. Adjoint Sensitivity techniques identify the state variables and geographic locations to which a chosen aspect is most sensitive. The location of greatest sensitivity is typically dynamically upstream (Zhang et al., 2009c) of the chosen aspect, and is presumably the most effective region to target with observations in order to improve prediction of the chosen aspect. Both adjoint sensitivity and singular vector approaches identify where new information would diminish forecast error in a DA system, but neither take into consideration existing or planned observations. Existing sustained operational data used in a DA system may project onto the singular vectors or occur near the dynamical upstream and will change the pattern of the most effective *new* observations. Where best to acquire new targeted observations to complement existing observations can be addressed in Observation Sensitivity and Ensemble Transform techniques.

The Observation Sensitivity approach determines the effect of each assimilated observation on the analysis and forecast of a chosen aspect using the adjoint of the data assimilation and forecast system so that the added information of hypothetical observations can be obtained. Ensemble Transform techniques use an ensemble of forecast simulations to retrieve the covariance of forecast and then seek the observation

pattern which best minimizes forecast uncertainty. It is most suitable for systems using ensemble-type data assimilation methods.

In contrast to meteorology, there are relatively few published studies of targeted observations in oceanography. Most recent studies employing data assimilation in oceanography emphasize state estimation, and to complement these targeted observation efforts have paid greatest attention to capturing certain ocean phenomena or variability (e.g. intra-seasonal variability in the tropical oceans) in an analysis, rather than a forecast. Examples are work utilizing ensemble transform type techniques (Ballabrera-Poy et al., 2007; Bennett, 1990; Hackert et al., 1998; Oke and Schiller, 2007; Sakov and Oke, 2008) to study the designs of tropical mooring arrays. Frolov et al. (2008) utilized a similar technique to assess fixed coastal and estuarine observatories. Barth and Wunsch (1990) used a simulated annealing technique to optimize an acoustic array design. Using the adjoint sensitivity technique, Shulman et al. (2005) identified the upstream of a bioluminescence patch and conducted survey accordingly. Based on array mode analysis, i.e. the eigen-analysis of the stabilized representer matrix (the sum of representer matrix and observational error matrix), McIntosh (1987) proposed the optimal positioning of tide gauges in an open-ended channel, and Bennett (1990) assessed an equatorial Pacific XBT observing program.

Köhl and Stammer (2004) simplified the observation sensitivity technique by assuming that model error is much smaller than observational error, and applied the approach to optimizing observation locations for determining heat transport across the Greenland-Scotland ridge. Targeted observation is typically followed by data assimilation, so Köhl and Stammer's (2004) assumption of large observational error is somewhat

contradictory and interpreting the result as observation sensitivity (as in Baker and Daley (2000)) is questionable. However, as we will show in the next section, the simplified technique is still consistent with computing the representer of the chosen aspect – it gives the covariance and then correlation between the chosen aspect and ocean state at all locations and times. Then it is logical to observe the places where the correlation is the highest, which concurs Köhl and Stammer's (2004) finding that their method is valid also when the observational error is small.

In New York Bight (NYB), local forces (e.g. topography, river discharge and air-sea exchange) and remote forces (e.g. large scale shelf circulation) interact on a wide continental shelf to create a coastal zone with complicated dynamics and short time and space scales of variability (Choi and Wilkin, 2007; Yankovsky, 2003; Zhang et al., 2009a). The region has been the subject of many studies, both modeling and observational (Castelao et al., 2008a; Chant et al., 2008a; Chant et al., 2008b; Johnson et al., 2003; Tilburg and Garvine, 2003; Wilkin et al., 2005; Wong, 1999; Yankovsky et al., 2000; Zhang et al., 2009a). The area has seen pioneering deployments of new observing instruments like autonomous underwater vehicles (gliders) (Schofield et al., 2007), coastal High-Frequency (HF) Radar systems (Kohut et al., 2006), cabled observatory moorings (Glenn et al., 2000), and the comprehensive use of multiple satellites (Schofield et al., 2004) together with ship-borne instruments during a series of intensive multidisciplinary observational programs (Chant et al., 2008b). The monitoring of water conditions in NYB is operated on a quasi-continuous base, which makes the NYB an ideal place to experiment with integrating observation and modeling capabilities.

Part I (Zhang et al., 2009b) of this study demonstrated the use of observations to correct a numerical model using 4DVAR data assimilation. Assimilating a variety of observations gave a better estimate of the ocean state and more skillful short-term forecasts. In this paper, Part II, we explore use of the model to objectively assess and guide observation strategies. It provides a prototype for forecast-oriented targeted observation in a coastal region. We stress here that we do not intend to use the targeted observations to interpret physics directly, but rather assimilate the data into a numerical model that will then capture the aspect of interest more precisely.

This paper is organized as follows: Section 2 describes the theory of representer-based observing system design; Section 3 describes the system setup; Section 4 applies the method to predicting salt flux within the Hudson Shelf Valley (HSV); Section 5 compares the influences of different observations; Section 6 summarizes the work.

2. Representer-based observing system design

Let us denote $\Phi(t)$ to be the ocean state vector $[\mathbf{u} \ \mathbf{v} \ \mathbf{T} \ \mathbf{S} \ \zeta]^T$ comprised of the velocity, temperature, salinity and sea surface height at all grid points at time t . A representer is the covariance between a single element of $\Phi(t_0)$ at a particular grid point at time t_0 , which we call a “point aspect of interest” in this paper, and all other elements of $\Phi(t)$ (a 3-dimensional field at time t) (Bennett, 2002; Kurapov et al., 2009). The covariance is not based on temporal variation of the ocean state but on different realizations of randomly distributed ocean states in Bayesian statistics (van Leeuwen and Evensen, 1996).

We can transform the continuous space-based representer formulation in Bennett (2002) to a discrete space-based matrix formulation as

$$\text{Representer} = \mathbf{MBM}^T \Delta(\phi_0, \mathbf{x}_0, t_0), \quad (1)$$

where \mathbf{M} is tangent linear model propagator and \mathbf{M}^T is the corresponding adjoint operator (Moore et al., 2004), \mathbf{B} is the background error covariance matrix, Δ is a impulse vector with the same length as Φ ,

$$\Delta(\phi_0, \mathbf{x}_0, t_0) = \begin{cases} 1 & \phi = \phi_0 \text{ and } \mathbf{x} = \mathbf{x}_0 \text{ and } t = t_0 \\ 0 & \phi \neq \phi_0 \text{ or } \mathbf{x} \neq \mathbf{x}_0 \text{ or } t \neq t_0 \end{cases},$$

ϕ_0 is the variable of interest ($\phi_0 \in [\mathbf{u} \ \mathbf{v} \ \mathbf{T} \ \mathbf{S} \ \zeta]^T$), \mathbf{x}_0 is the location of interest, and t_0 is the time of interest. Then $\phi_0(\mathbf{x}_0, t_0)$ is the point aspect of interest.

This representer is based on the linearization around a nonlinear model trajectory embodied in the tangent linear and adjoint models. In variational data assimilation, if the aspect of interest is the ocean state at a single observation location, the representer describes the influence of the observation in the model (Bennett, 1990; Egbert and Erofeeva, 2002; Kurapov et al., 2009). To obtain a representer described by (1), an adjoint model is initialized with $\Delta(\phi_0, \mathbf{x}_0, t_0)$ and integrated backward in time, the background error covariance is applied, and a forward integration of a tangent linear model concludes the computation. Here, $\Delta(\phi_0, \mathbf{x}_0, t_0)$ can be considered as $\partial J_0 / \partial \Phi(t_0)$, where J_0 is an objective function of a point aspect of interest, $J_0 = \phi_0(\mathbf{x}_0, t_0)$. Hence, the representer gives the covariance between J_0 and $\Phi(t)$, and (1) becomes

$$\text{rep}\left(\frac{\partial J_0}{\partial \Phi(t_0)}\right) = \mathbf{MBM}^T \frac{\partial J_0}{\partial \Phi(t_0)} = \text{cov}(J_0, \Phi(t)). \quad (2)$$

Here we denote the linear representer operator as $\text{rep}(\cdot)$. Notice that the units of (2) are $[J] \cdot [\Phi]$. The middle term in (2) is similar to Equation (13) in Köhl and Stammer (2004)

except for the sampling operator and observation error covariance matrix that they applied after the representer.

Next, we extend the representer concept to more general circumstances. For a and b being any two independent point aspects of interest at time t_0 , it can be shown (see Appendix) that

$$\text{Crep}\left(\frac{\partial(a+b)}{\partial\mathbf{\Phi}(t_0)}\right) = \text{cov}(a+b, \mathbf{\Phi}(t)), \quad (3)$$

$$\text{Crep}\left(\frac{\partial(a-b)}{\partial\mathbf{\Phi}(t_0)}\right) = \text{cov}(a-b, \mathbf{\Phi}(t)), \quad (4)$$

$$\text{Crep}\left(\frac{\partial(ab)}{\partial\mathbf{\Phi}(t_0)}\right) \square \text{cov}(ab, \mathbf{\Phi}(t)), \quad (5)$$

and

$$\text{Crep}\left(\frac{\partial(a/b)}{\partial\mathbf{\Phi}(t_0)}\right) \square \text{cov}(a/b, \mathbf{\Phi}(t)). \quad (6)$$

Here, $\text{Crep}(\cdot)$ denotes the combination of some representers. Note that we refer the superposition of some representers as *combination of representers* in this paper to draw the difference between the representer of a single observation and the covariance information given by superposition of a group of representers.

Given equations (3) – (6), it follows that

$$\text{Crep}\left(\frac{\partial J}{\partial\mathbf{\Phi}(t_0)}\right) = \text{cov}(J, \mathbf{\Phi}(t)) \quad (7)$$

holds true for J defined as a combination of arithmetic operations on ocean state variables at time t_0 . For J constructed as a sum of contributions from several snapshots

over certain time interval, $J = J(\Phi(t))$, $t \in [t_1, t_0]$, the associated combination of representers can be simply obtained as a sum of individual representers because the system is linear. Equation (7) is thus still valid.

Provided the aspect of ocean dynamics of interest can be expressed as an arithmetic function of model variables, e.g. salt transport across a certain cross-section, we can compute a combination of representers to give the covariance between the aspect of interest and ocean variables at all locations at any time in the integration window. The only limitation is that linearity assumption holds for the duration of the integration time window (Zhang et al., 2009b).

Suppose observations are to be gathered in order to determine some aspect of regional ocean dynamics, with no other observations being available for this purpose. It is logical to deploy instruments at the place where the state variables have the highest correlation with the aspect of ocean circulation that is of interest. Assimilation of these observations into the model will lead to more precise description of the aspect of interest. Note that a representer extends over times that precede, span, and follow the interval when the aspect of interest, J , is defined. Hence, representer-based observing system design can guide data acquisition for forecasting, nowcasting and re-analysis.

3. System setup

3.1. Model configuration

The Regional Ocean Modeling System (ROMS, www.myroms.org), a free-surface, hydrostatic, primitive equation model, is used in this study. It consists of nonlinear forward, tangent linear and adjoint models and numerous drivers that utilize the

component models for adjoint sensitivity, optimal perturbation, representer-based optimal observation, observation sensitivity, and 4DVAR data assimilation applications (Broquet et al., 2009; Di Lorenzo et al., 2007; Moore et al., 2008; Moore et al., 2004; Powell and Moore, 2008; Powell et al., 2008a; Powell et al., 2008b; Zhang et al., 2009c).

The model domain (Figure 1) extends from south of Delaware Bay northeastward to eastern Long Island. Two major rivers are included: the Hudson and Delaware. The model has 30 terrain-following vertical layers and 2 km horizontal resolution. The nonlinear forward control simulation with respect to which the tangent linear and adjoint models are linearized covers the year 2006 with initial conditions from Zhang et al. (2009a). It uses Chapman (1985) and Flather (1976) conditions for sea level elevation and the barotropic component of velocity on the model open boundaries, respectively. Steady along-shelf flow (Lentz, 2008) and tidal elevation and current (harmonic constituents K1, O1, Q1, M2, S2, N2, K2) extracted from a regional simulation (Mukai et al., 2002) were imposed on the open boundaries. Orlanski-type radiation conditions (Orlanski, 1976) were applied for 3D velocity and tracers. Vertical mixing was parameterized with the k - kl scheme of general length scale method (Umlauf and Burchard, 2003; Warner et al., 2005) and quadratic bottom drag was used with drag coefficient 0.003. At the sea surface, bulk formulae (Fairall et al., 2003) with meteorological conditions from the North American Regional Reanalysis (Mesinger et al., 2006) were applied to compute air-sea momentum and heat exchange. River discharges were obtained from USGS Water Data (<http://waterdata.usgs.gov/nwis>) and scaled to include ungauged portions of the watershed.

3.2. Representer computation

In Section 2 it was outlined how computation of the representer described by (1) involves integration of an adjoint model backward in time (typically 3 or 4 days in our applications), application of a background error covariance, \mathbf{B} , and forward integration of a tangent linear model. The adjoint forcing, $\partial J/\partial \Phi(t)$, is applied to the time interval over which J is defined. The duration of the adjoint and tangent linear model integrations depends on the processes of interest, but is also constrained by the period for which the linearization holds. Zhang et al. (2009c) tested the linearity assumption in a model with the same domain but a higher horizontal resolution (1 km) and found that it is valid for 3 days. Their tests were rather strict (varying initial conditions with the fastest growing anomaly pattern obtained from optimal perturbation theory), and model resolution in this study is lower, so we expect the linear assumption to be valid at least as long and almost certainly for a longer duration window. In the application presented below analyzing salt flux within the HSV, we integrated adjoint model backward for 4 days in order to consider the design of AUV glider deployments 2 days prior to the defined J .

The background error covariance acknowledges correlations between the same variable (univariate) and different variables (multi-variate) at different locations due to dynamical scales and processes. At the time of this study ROMS implements only a univariate \mathbf{B} . It is simulated by solving two diffusion equations (one for horizontal and the for vertical) that impose decorrelation scales chosen here to be 20 km in the horizontal and 2 m in the vertical. Detailed descriptions of how the background error covariance is treated in ROMS are given by Powell et al. (2008b) and Broquet et al. (2009).

Before proceeding to an analysis of representers constructed to aid observing system design in the NYB, we illustrate the interpretation of a simple representer computed for a single observation point. Figure 2 (top row) shows surface during 5 days in September 2006. The aspect of interest, J , for the purposes of illustration was chosen to be salinity at position $\mathbf{x}_0 = 73.7^\circ\text{W}, 40.3^\circ\text{N}$, (indicated by the triangle symbol in Figure 2) at $t_0 = 2006-09-18\ 00:00\ \text{UTC}$. To compute the representer for this simple J the adjoint model is forced by a delta function in salinity at the place of interest, i.e. $\partial J / \partial \Phi(t_0) = \delta(S, \mathbf{x}_0, t_0)$. Here, we integrate backward for 4 days then apply the univariate background error covariance with the length scales noted above. Figure 2 (bottom row) shows the time evolution of surface salinity in the subsequent tangent linear model – the surface salinity representer for this J .

The modeled salinity shows that the river plume has two branches. One branch curls southeastward having detached from the Long Island coast, while the other fresher branch flows southward along the New Jersey coast. The higher salinity water between them is a shoreward intrusion of mid shelf water along the HSV (Zhang et al., 2009a). On 2006-09-18 00:00 UTC, the tip of the southwestward flowing branch reaches \mathbf{x}_0 . Transport pathways strongly influence salinity patterns in the NYB (Zhang et al., 2009a) so we expect properties of water at the point of interest to be correlated with properties in the two plume branches. The surface salinity representers show these patterns. At 2006-09-14 00:00 UTC, just after applying the background error covariance, the surface salinity representer has a circular pattern of high covariance in the New York Bight apex centered on a location clearly different from \mathbf{x}_0 . The circular shape of the pattern stems from the smoothing effect of the background error covariance. The pattern subsequently

transforms as the tangent linear model integration proceeds. By 2006-09-18 00:00 UTC, the time at which the aspect of interest is defined, the representer shows surface covariance develops a two-branch pattern with similarities to the plume. The highest covariance, not surprisingly, occurs near the point of interest itself, and decays proceeding upstream back along the plume trajectory. The covariance with the other branch along the New Jersey coast is lower but still greater than in the intervening region influenced by higher salinity mid-shelf waters. The two branches are connected at the estuary entrance.

The surface salinity representer has identified the area that, 4 days prior, supplies water to the point of interest, but has also identified that the same region is a source of water to the New Jersey coastal current at this time. Couched in terms of data assimilation, the representer indicates that observations made at the point of interest would impact the assimilation increments in both branches of the flow emanating from New York harbor.

Figure 3 shows vertical cross-sections of the salinity representer at 2006-09-18 00:00 UTC along lines A and B in Figure 2. In both cross-sections covariance is greatest in the surface 15 m and around the point of interest. The 15 m depth corresponds to the depth of the surface mixed layer in this area. Cross-section A shows a pattern extending into the estuary, but there the covariance falls to zero at the surface while remaining positive near the bottom. This occurs because recently discharged low salinity river water at the surface is independent of the previously discharged waters that flow onward to the point of interest. In cross-section B (Figure 3b), which cuts across the HSV and bridges the two freshwater branches, the representer shows high covariance at both ends and zero

between because the shoreward intrusion of mid-shelf water along the HSV (Zhang et al., 2009a) has a different source from the water on either side.

The representer shows above, associated with a simple point aspect of interest, gives covariance patterns readily interpreted in terms of the local circulation and is presented here in order to develop some experience in how to interpret the results. Next, we turn our attention to formulating representers that will aid the design of observing strategies.

4. Targeted observations

4.1. Background

Flow variability within the HSV is correlated with local wind and sea level elevation (Mayer et al., 1982; Nelson et al., 1978) and the mean flow in the valley is shoreward (Zhang et al., 2009a). Because of seasonal variation in the wind, stratification, and possibly the remotely forced along-shelf circulation, the shoreward ocean water intrusion in the HSV intensifies in winter (Harris et al., 2003; Nelson et al., 1978). Figure 4 shows seasonal averages of the salinity and current at 20 m from the nonlinear forward simulation of 2006. At the cross-section indicated by the short black line the current at 20 m is shoreward along the valley in spring and winter with the strongest intrusion in winter. In summer and fall, the circulation at the cross-section is roughly parallel to the isobaths crossing the valley. Figure 5 shows time series of the vertically integrated subsurface (below 10 m) salt flux across the cross-section over 2006. It is evident that shoreward salt flux dominates the spring and winter seasons and the time period (October - April) is consistent with observations by Nelson et al. (1978). Shoreward flow in the HSV transports salty, high nutrient subsurface ocean water towards the inner shelf where

it mixes or upwells to the surface, with consequences for local biogeochemical processes. The shoreward flow in the HSV also carries resuspended sediment onshore (Harris et al., 2003; Manning et al., 1994).

4.2. Representer-based glider track design

Given the influence of circulation in the HSV on local biogeochemistry and sedimentation, detailed knowledge of the transport within the HSV is relevant to many processes. Rutgers University Coastal Ocean Observation Laboratory (RU-COOL) commonly operate gliders in this area, so we have formulated an example of representer-based observing system design in this section aimed at evaluating optimal tracks for glider missions. The question we ask is: where should we deploy gliders in order to better predict, 2 days in the future, the along-valley salt flux across a selected cross-section? The cross-section we choose is indicated by the short lines plotted in Figure 4. To answer the question we define the objective function, J , as the vertically integrated subsurface salt flux 2 days after the glider deployment, and we are going to apply the representer system to obtain the covariance and then correlation between J and variables everywhere at the deployment time. Observations made where and when the correlation is the highest should have the greatest impact on the model-based analysis. As mentioned previously, we assume there are no other observations in the environs of the cross-section.

The work flow of the representer-based observation design system is depicted in Figure 6. Firstly, a forward nonlinear simulation (control run) is carried out and we assume the simulated result is the truth. Secondly, J_t , the “true” subsurface salt flux through the cross-section averaged over 1 day (the 4th day after nominal time zero) and the corresponding adjoint forcing, $\partial J/\partial \mathbf{\Phi}(t)$, are computed from the control run. Thirdly,

a representer computation is conducted with 4-day adjoint model integration and 1-day tangent linear model integration. This gives the covariance field at day = 1, two days prior to the interval over which J is defined. Steps 2 and 3 were then repeated with the nominal day = 0 advanced by two days at a time over the entire period of 2006 until a total of 180 combinations of representers were computed. This ensemble of combinations of representers was grouped into two sets for spring-winter (October – April) and summer-fall (May – September). The correlation associated with each salinity representer was then obtained by normalizing by the product of the standard deviations of J and detided model variables. The RMS of all the correlation fields in each set was then computed and the result at 20 m depth is presented in Figure 7.

The average correlation map for summer-fall (Figure 7a) has highest correlation north of the cross-section and the correlation contours are near circular. In winter-spring, the highest correlation occurs east of the cross-section and is elongated roughly alongshelf. These positions are consistent with the circulation in Figure 4. In summer and fall, subsurface current is southward to southwestward, so the upstream of the cross-section is somewhere to the north. In winter and spring, circulation at the cross-section is shoreward along the HSV and the upstream of the cross-section is to the east or southeast. Moreover, the correlation in winter-spring season is much higher because the current within the HSV is much stronger at that time.

Guided by the information in the correlation patterns we designed optimal glider tracks for each biseasonal period and present these in Figure 7 (triangles) along with a traditional design approach that would simply operate gliders on both sides of the cross-section (circles). We emphasize that the optimal track is not obtained from a robust

optimization algorithm but designed intuitively according to the correlation pattern. We call it “optimal” here to distinguish it from the traditional track. True optimization would be based on a mathematical algorithm that took into consideration constraints on glider operation.

4.3. Twin experiments

We evaluate whether the proposed optimal sampling strategy is indeed advantageous with a set of data assimilation twin experiments, the work flow for which is depicted in Figure 6. For each member in the ensemble we took temperature and salinity vertical profiles from the control run along the two tracks (optimal and traditional). The optimal track was chosen according to the season. Both sets of “observations” were taken on the second day from the nominal time zero (Figure 6), and had the same quantity of data to make the comparison fair. We then conducted a perturbed nonlinear forward simulation by starting from the end of day = 1 with initial conditions obtained from the model state 5 days prior (day = -4 in Figure 6). Forcing was unchanged from the control run. The subsurface salt flux at the cross-section at day = 4, J_b , therefore differs from the truth, J_t . Incremental Strong-constraint 4DVAR (IS4DVAR) data assimilation, using the same approach described in Part I (Zhang et al., 2009b) was used to assimilate the two sets of observations. The data assimilation window is 1 day and the “glider-measured” temperature and salinity profiles were the only data assimilated. The adjusted initial conditions given by the two data assimilation analyses were used to initialize two forecast simulations. For the 180 members of the ensemble we therefore have the true salt flux at the section at day = 4, J_b , the prior conditions to the data assimilation from the perturbed

simulation, J_b , and two forecast realizations (one each for the optimal and traditional sampled data sets), which we denote J_a .

The forecast skill of the data assimilation system for the two data sets is presented in Figure 8 using a forecast skill metric defined as

$$S = 1 - \frac{|J_a - J_t|}{|J_b - J_t|}. \quad (8)$$

When $S > 0$, data assimilation has improved the forecast J compared to the prior value. The larger the value of S , the better the prediction. For both seasons, the system assimilating optimally sampled observations gives a statistically better 2-day prediction of the salt flux. In summer-fall the improvement in J for the optimal track is comparable to the one obtained with the traditional tracks, but for winter-spring the improvement in the prediction using optimal tracks is substantial. Figure 8 also shows that assimilating the optimal observations does not necessarily give better prediction of the salt flux for other days; e.g. in winter-spring the first day predictions of salt flux of the two systems are indistinguishable. This highlights that the definition of objective function is important in the representer-based observing system design.

5. Comparison of observation influences

Observation influence is a measure that operational oceanographers and policy makers discuss with regard to integrating observing systems (Kaiser and Pulsipher, 2004), designing new observation networks (Oke and Schiller, 2007), or evaluating existing observations (Frolov et al., 2008). In this section we explore the use of the representer system to compare observation influences.

In Section 2 we discussed how the representer associated with a single observation describes the influence of that observation in a 4DVAR data assimilation system. We also expanded the representer concept to broader circumstances of arithmetic functions of state variables. Here we follow a similar approach to consider the influence of a set of many observations, of multiple state variables, on data assimilation.

Suppose we have a numerical model and a group of observations. Because of errors in initial conditions, boundary conditions, forcing, or model physics, the model results differ from their observed equivalent. A direct gain of merging the observations and model is correction of the model error at the observation locations and times. If the model error is known, we can quantify the gain by defining a gain function, J . The gain function of a single observation is the model error at the observation location, that is, $J_0 = \phi_0(\mathbf{x}_0, t_0) - \phi_t(\mathbf{x}_0, t_0)$, where $\phi_0(\mathbf{x}_0, t_0)$ is observed quantity in the model and $\phi_t(\mathbf{x}_0, t_0)$ is the truth. The gain function of a group of observations can be the superposition of the gain functions of each individual observation and therefore an arithmetic function of model errors. In a 4DVAR system, assimilating the observational data corrects not only the observed state variables at the observation locations and times but also the model state at other locations and times through the dynamical and statistical connections that are embedded in the system. The extended influence of the observations is what we intend to quantify.

The initial condition, $\Delta(\phi_0, \mathbf{x}_0, t_0)$, to the adjoint model in computing the representer of a single observation can be considered as the derivative of the corresponding gain function with respect to model state everywhere at the observation time, $\partial J_0 / \partial \Phi(t_0)$. The resulting representer gives the covariance of J_0 and model states everywhere at all

locations, and therefore outlines the influences of the observation in a 4DVAR system (Bennett, 2002). For a group of observations, whose gain function can be expressed as superposition of the gain functions of each observation, we can obtain their influences in a 4DVAR system by combining the representers associated with each observation because the representer system is linear. The mathematical basis for this is essentially the same as in Section 2.

We present three examples to demonstrate representer-based analysis of observation influence. We consider (i) the area and strength of influence of two different observing strategies, (ii) how the same observation strategy has differing influence for different dynamical regimes, and (iii) how the influence of a given set of observations alters with different data assimilation windows. Note that the comparison in this study is not for the design of a realistic observation network, but rather is presented to illustrate and understand what a representer system can offer and to qualitatively compare the influences of some elementary components of an observational system.

5.1. Comparison of glider and mooring observations

Gliders and moorings are two instrument platforms commonly deployed in the NYB to measure vertical profiles of temperature and salinity. We compare their influences in this section. Figure 1 shows a track typical of the so-called ‘Endurance Line’ cross-shelf glider section routinely surveyed approximately 10 times per year by the RU-COOL (Castelao et al., 2008a). Here we consider a hypothetical glider transect slightly north of the nominal real track and assign the one-way mission to be 3 days in duration which is roughly the time it takes a real glider to traverse the shelf. In comparison, we consider a

hypothetical mooring located at the 20 m isobath on the hypothetical glider track that observes temperature and salinity throughout the water column.

Our analysis uses 60 days of simulated ocean conditions in April and May, 2006, from the forward control simulation introduced in Section 3. Full water column vertical temperature and salinity profiles were sampled from the control model at every model time step (180 seconds); at a single fixed location in the case of the mooring, and at locations traversing the shelf over 3 days in the case of the glider. The 2-month period was then separated to twenty 3-day windows and a representer computation was conducted in each window. Assuming model error everywhere is proportional to ocean state anomaly and with the constant scale between model error and ocean state anomaly neglected, we define the gain function as an overall measure of the model error at the observation locations and times,

$$J = \frac{1}{N} \sum_i^N \left[\frac{(T_i - \bar{T}_i)^2}{\mathbf{O}_{Ti}} + \frac{(S_i - \bar{S}_i)^2}{\mathbf{O}_{Si}} \right], \quad (9)$$

where N is the total number of samples, T_i and S_i are observed temperature and salinity, respectively, the overbar denotes temporal mean at each observation location, \mathbf{O}_{Ti} and \mathbf{O}_{Si} are error covariance of each temperature and salinity observation, respectively. This definition of gain function is similar to the observational cost function of 4DVAR data assimilation (Part I). With this definition, the influence of each observation in the group is essentially scaled by the model error at the observation location and time. The resulting total influences ought to be explained as model-error-scaled influences of the group observations.

The representer computation is as in Section 4. For each combination of representers, the adjoint model is integrated backward for 3 days with adjoint forcing, $\partial J/\partial \Phi(t)$, throughout the integration period, the background error covariance is applied at the nominal $t = 0$ for the interval, and the tangent linear model is integrated for 6 days to show the observation influences in both analysis (the first 3 days) and forecast (the last 3 days) periods. The RMS of the ensemble of 20 covariance fields was then computed for different relative times in the 6-day window. Figure 9 shows the RMS average temperature covariance at the surface through time.

In the analysis period (the first two columns in Figure 9) the glider observations have influence over a wider area than the mooring, but the strength of influence of the mooring at the observation location is about twice that of the glider. This result is consistent with most oceanographers' intuition on the likely relative value of the two instruments, but is quantified by the representer analysis. During the forecast period (the last two columns in Figure 9), the influence of the glider observations decays, while that of the mooring stays strong. At day 6, 3 days into the forecast, the influence of the mooring at the observation location is more than 3 times stronger than that of the glider. Moreover, the area of influence of the mooring expands quickly along the shelf over the forecast period, but that of glider observation expands little. At day 6, it does not appear that the glider has greater or lesser overall influence than the mooring.

In Figure 10, we plot the influence of data from the two instruments along the vertical cross-section along the glider track. As inferred from Figure 9, the glider influence extends across the shelf while the mooring has greater magnitude but less spatially extensive influence centered at the observation location. An interesting feature in Figure

10 is that both cross-sections at day 0 show rather greater influence in the surface and bottom boundary layer than in the middle of the water column. This suggests that dynamical connections in the boundary layers, caused by the wind-driven coastal upwelling and down-welling, extend the scope of influence of observations – a consequence of the ocean physics embodied in the adjoint and tangent linear models.

5.2 Influence of glider observations in different wind regimes

Wind-driven coastal upwelling and down-welling are common phenomena in the inner shelf of the NYB (Castelao et al., 2008b; Wong, 1999; Yankovsky and Garvine, 1998), and effective observational strategies for these distinct dynamical regimes are of interest to operational oceanographers. In this section we take the hypothetical glider section in Section 5.1 as an example and demonstrate how its influence differs in upwelling and down-welling regimes.

The 20 combinations of representers of glider in Section 5.1 were separated into two groups according to the average wind direction in the 3-day observation windows (southerly wind drives upwelling on the New Jersey coast; northerly wind drives down-welling), and RMS of the temperature covariance field of each group, at the sea surface, is presented in Figure 11.

The influence in the analysis window (days 0 to 3) during upwelling is about twice as strong as that in the down-welling regime. Because coastal upwelling pulls deep cold water up to the surface and down-welling pushes offshore surface water on shore, surface temperature anomaly associated with upwelling is stronger. Model surface temperature error in the upwelling regime is consequently larger since the combination of representers

computed here is the model-error-scaled influence. Therefore, the influence of the glider observations in upwelling regime on correcting model errors is accordingly larger.

At day 0, the area of influence of the observations extends further southward along the coast in the upwelling regime and further northward in the down-welling regime. This reflects that the model captures the dynamical upstream of the observed quantities, and this will subsequently influence the 4DVAR assimilation system. During upwelling, coastal surface water to the south of the glider track advects northeastward and, therefore, surface glider observation at the end of the 3-day window actually include information about the properties of the coastal surface water to the south back to day 0. During down-welling, surface water north of the glider track is pushed toward the coast where it subducts and flows southward. Subsurface glider observations at the end of the analysis window thus capture properties of coastal surface water north of the track at day 0. The upstream information embodied in the observations and revealed by the representer analysis concurs with the identification of dynamical upstream regions by adjoint sensitivity (Zhang et al., 2009c). As time proceeds into the forecast window (the last two columns in Figure 11), the area of influence propagates in the respective downstream direction for the two regimes.

5.3 Comparison of different data assimilation windows

An advantage of 4DVAR data assimilation is its ability to propagate information, e.g. observation innovation, over time, both backward and forward. Ideally, we would like the information to be propagated as long as possible in order to fully exploit the dynamical connections captured by the adjoint and tangent linear models. But the duration the information can propagate, the data assimilation window, is somewhat constrained by the

linearization assumption in 4DVAR systems. For the same observations, different lengths of the data assimilation window will result in different observation influence. To show this, we present a simple example using the representer-based estimate of observation influence.

We formed 4 groups of combinations of representers for observations along the hypothetical glider track. Each group has 20 combinations of representers. The adjoint models in the 4 groups were initialized at the same times and integrated for 0, 1, 2 and 3 days, respectively, and the tangent linear models were integrated for 3, 4, 5 and 6 days, respectively. To make the comparison fair, we assumed all glider observations we made at the instant of the initial times of the adjoint models; this ensured all representer windows received equivalent amounts of data.

The RMS of the covariance fields in each group was computed and from these the average surface temperature influences are presented in Figure 12. Day = 3 is the observation time in each representer computation, and day = 6 is the ending time of the tangent linear integration (3 days after observations). Comparing the plots in each row shows that the longer the window is the larger the area of influence. At day 3, the average influence in the 0-day window group is confined around the glider track and results almost entirely from the background covariance immediately extending the observational information to neighboring points. As the window becomes longer, the influence spreads out, especially along the coast, reflecting the added information introduced by the adjoint and tangent linear models in regions that are dynamically upstream to the data locations. The average influence in the 3-day window group covers almost the entire New Jersey coast. Note that the small covariance value (0.01) at the

edges of the area of influence results from the ensemble averaging process. The covariance in any individual combination of representers is larger, but with area of influence that is smaller and skewed toward the upstream region for the flow at that particular time.

The combination of representers of the 0-day window is analogous to observation influences in sequential data assimilation, e.g., 3DVAR and Kalman filter-type data assimilation methods. In those methods information about the dynamical upstream is not exploited; there is no backward in time propagation of observation innovation. In 4DVAR data assimilation, the adjoint model propagates the observation innovation backward according to the linearized dynamics and identifies where corrections should be made to the dynamically upstream initial conditions, boundary conditions, or surface forcing. The Kalman smoother shares some of these properties.

6. Summary

This paper is the second part of a project to build an integrated observation and modeling system for the New York Bight for the purposes of coastal ocean prediction and observing system design. Part I demonstrated how 4DVAR data assimilation using ROMS improves ocean state estimates in a realistic pseudo-real-time setup. This Part is dedicated to the complementary objective of using an integrated observation-modeling system to improve observing system design.

A representer function describes the covariance between a point aspect of interest and variables at all locations at any time. In 4DVAR data assimilation, the representer expresses the influence of a single assimilated observation and can be used in the process

of cost function minimization in observation space (Bennett, 2002). To extend the application of the representer beyond an isolated observation, we have shown that the combination of representers associated with an arithmetic function of model variables has properties similar to an isolated observation. It describes the covariance between the aspect of interest described by the arithmetic function and model variables at all locations at any time. Where the correlation is the highest is logically a more optimal place to acquire observations in order for the model to describe the aspect of interest more precisely. Applying the same theory to observation influence, we showed that the combination of representers associated with a group of observations outlines the influence of the observations as a whole in a 4DVAR data assimilation system.

For the simple case of a representer associated with a point aspect of interest in the Hudson River plume, we noted consistency between the representer pattern and the recognized local dynamics of transport pathways for the plume.

Considering the design of observational strategies, we sought an “optimal” glider track for better model prediction of salt flux across a cross-section of the Hudson Shelf Valley 2 days after the glider deployment. An ensemble of combinations of representers were computed and grouped into two biseasonal periods (summer-fall, and winter-spring) that share similar characteristics in the mean circulation. Optimal glider tracks were then picked heuristically for both seasons according to the correlation maps. Data assimilation twin experiments verified that glider observations taken along the proposed ‘optimal’ paths led to greater skill in term of predicting the salt flux 2 days after the observations were obtained.

A representer-based system was presented that measures the influence of a group of observations in a 4DVAR data assimilation system, and this was used to compare the data influence for different observing strategies. We compared the influences of equivalent amounts of data acquired by a repeat glider cross-shelf section versus a fixed mooring. The glider section has a wider area of influence while the mooring has stronger influence in the environs of the observation location.

We compared the influence of the same routine glider section in different dynamical regimes: wind-driven coastal upwelling and down-welling. The area of influence of the glider data is shifted toward the dynamical upstream: southward along the coast in upwelling and northward along the coast in down-welling. We evaluated the influence of duration of data assimilation window lengths, obtaining a result that agrees with intuition that a longer assimilation window introduces more dynamical connections and extends the influence of observations to a larger area.

This work demonstrates the capability of representer-based systems to aid in developing more optimal observation strategies and quantifying the extent of influence of a set of observations. The method can be used to help design the positioning of a single instrument or an observation network. We emphasize that the notion of what observing strategy is optimal depends on the quantity of interest, but the system we have described is flexible in its ability to consider quite arbitrary arithmetic functions of the ocean state, including fluxes and transports, and regional spatial means or time averages.

The work in this paper approaches the design problem from one perspective; namely, identifying observing system characteristics that enhance forecast skill when the data are subsequently adopted in a 4DVAR assimilation system. True optimization of observing

system design must take in to consideration other constraints that are instrumental and logistical.

Appendix: Derivation of equation (3) – (6)

Suppose a and b are two independent variables at particular locations of interest, \mathbf{x}_1 and \mathbf{x}_2 respectively, at time t_0 , that is, $a = \phi_1(\mathbf{x}_1, t_0)$ and $b = \phi_2(\mathbf{x}_2, t_0)$, and N is the number of all possible ocean states. We have two assumptions: (i) the ocean state given by the control nonlinear simulation is a valid estimate of the ensemble mean of a set of ocean states, that is, $a_0 = \bar{a}$, and $b_0 = \bar{b}$, where subscript 0 stands for the value given by the control simulation and overbar the ensemble mean; (ii) the deviation of all possible ocean states from the mean is small and the product of two or more state deviations (e.g. $a'b'$) is negligible. The first assumption is valid because distribution of model errors is usually assumed to be Gaussian and the nonlinear model state around which the tangent linear and adjoint models are linearized is usually the best ones that can be obtained. The second assumption agrees with the small background error assumption we have in variational data assimilation. Overhead bars in following derivation stands for the mean of the randomly distributed ocean states.

Derivation of equation (3):

$$\begin{aligned}
 \text{Crep}\left(\frac{\partial(a+b)}{\partial\Phi(t_0)}\right) &= \text{rep}\left(\frac{\partial a}{\partial\Phi(t_0)}\right) + \text{rep}\left(\frac{\partial b}{\partial\Phi(t_0)}\right) \\
 &= \text{cov}(a, \Phi(t)) + \text{cov}(b, \Phi(t)) \\
 &= \frac{1}{N} \sum_{i=1}^N \left[(a_i - \bar{a})(\Phi_i(t) - \overline{\Phi(t)}) \right] + \frac{1}{N} \sum_{i=1}^N \left[(b_i - \bar{b})(\Phi_i(t) - \overline{\Phi(t)}) \right] \\
 &= \frac{1}{N} \sum_{i=1}^N \left[(a_i + b_i - (\bar{a} + \bar{b}))(\Phi_i(t) - \overline{\Phi(t)}) \right] \\
 &= \text{cov}(a+b, \Phi(t))
 \end{aligned}$$

Derivation of equation (4) is very similar to that of equation (3) and therefore neglected here.

Derivation of equation (5):

$$\text{Crep}\left(\frac{\partial(ab)}{\partial\Phi(t_0)}\right) = b_0\text{rep}\left(\frac{\partial a}{\partial\Phi(t_0)}\right) + a_0\text{rep}\left(\frac{\partial b}{\partial\Phi(t_0)}\right).$$

Applying aforementioned assumptions, we have

$$\begin{aligned} \text{Crep}\left(\frac{\partial(ab)}{\partial\Phi(t_0)}\right) &= \bar{b} \text{cov}(a, \Phi(t)) + \bar{a} \text{cov}(b, \Phi(t)) \\ &= \frac{1}{N} \sum_{i=1}^N \left[(\bar{b}(a_i - \bar{a}) + \bar{a}(b_i - \bar{b})) (\Phi_i(t) - \overline{\Phi(t)}) \right] \\ &= \frac{1}{N} \sum_{i=1}^N \left[(a_i \bar{b} + \bar{a} b_i) (\Phi_i(t) - \overline{\Phi(t)}) \right] \\ &= \frac{1}{N} \sum_{i=1}^N \left[(\bar{a} \bar{b} + a_i \bar{b} + \bar{a} b_i + a_i b_i - \bar{a} \bar{b} + \bar{a} b_i) (\Phi_i(t) - \overline{\Phi(t)}) \right] \\ &= \frac{1}{N} \sum_{i=1}^N \left[(a_i b_i - \bar{a} \bar{b}) (\Phi_i(t) - \overline{\Phi(t)}) \right] \\ &\square \text{cov}(ab, \Phi(t)) \end{aligned}$$

Derivation of equation (6):

$$\text{Crep}\left(\frac{\partial(a/b)}{\partial\Phi(t_0)}\right) = \frac{1}{b_0} \text{rep}\left(\frac{\partial a}{\partial\Phi(t_0)}\right) - \frac{a_0}{b_0^2} \text{rep}\left(\frac{\partial b}{\partial\Phi(t_0)}\right).$$

Applying aforementioned assumptions, we have

$$\begin{aligned}
\text{Crep}\left(\frac{\partial(a/b)}{\partial\Phi(t_0)}\right) &= \frac{1}{b} \text{cov}(a, \Phi(t)) - \frac{\bar{a}}{b^2} \text{cov}(b, \Phi(t)) \\
&= \frac{1}{N} \sum_{i=1}^N \left[\left(\frac{a'_i}{b} - \frac{\bar{a}b'_i}{b^2} \right) (\Phi_i(t) - \overline{\Phi(t)}) \right] \\
&= \frac{1}{N} \sum_{i=1}^N \left[\left(\frac{\bar{a} + a'_i}{b} - \frac{\bar{a}b'_i + a'_ib'_i}{b^2} - \frac{\bar{a} + a'_i}{b} + \frac{\bar{a}b'_i + a'_ib'_i}{b^2} \right) (\Phi_i(t) - \overline{\Phi(t)}) \right] \\
&= \frac{1}{N} \sum_{i=1}^N \left[\left(\frac{\bar{a} + a'_i}{b} \left(1 - \frac{b'_i}{b}\right) - \frac{\bar{a} + a'_i}{b} \left(1 - \frac{b'_i}{b}\right) \right) (\Phi_i(t) - \overline{\Phi(t)}) \right]
\end{aligned}$$

For $|b'_i/\bar{b}| < 1$, we apply Taylor series expansion and get

$$\begin{aligned}
\text{Crep}\left(\frac{\partial(a/b)}{\partial\Phi(t_0)}\right) &\square \frac{1}{N} \sum_{i=1}^N \left[\left(\frac{\bar{a} + a'_i}{b} \frac{1}{1 + \frac{b'_i}{b}} - \frac{\bar{a} + a'_i}{b} \frac{1}{1 + \frac{b'_i}{b}} \right) (\Phi_i(t) - \overline{\Phi(t)}) \right] \\
&\square \frac{1}{N} \sum_{i=1}^N \left[\left(\frac{a_i}{b_i} - \frac{\bar{a}_i}{\bar{b}_i} \right) (\Phi_i(t) - \overline{\Phi(t)}) \right] \\
&= \text{cov}(a/b, \Phi(t))
\end{aligned}$$

Acknowledgments

This work was funded by National Science Foundation grant OCE-0238957.

ROMS model development is funded by the US Office of Naval Research and National Science Foudation.

References

- Baker, N. and R. Daley, 2000: Observation and background adjoint sensitivity in the adaptive observation-targeting problem. *Q. J. R. Meteorol. Soc.*, **126**, 1431-1454.
- Ballabrera-Poy, J., E. Hackert, R. Murtugudde, and A. J. Busalacchi, 2007: An observing system simulation experiment for an optimal moored instrument array in the tropical Indian Ocean. *J. Clim.*, **20**, 3284-3299.
- Barth, N. and C. Wunsch, 1990: Oceanographic experiment design by simulated annealing. *J. Phys. Oceanogr.*, **20**, 1249-1263.
- Bennett, A. F., 1990: Inverse methods for assessing ship-of-opportunity networks and estimating circulation and winds from tropical expendable bathythermograph data. *J. Geophys. Res.*, **95**, 16,111-16,148.
- , 2002: *Inverse Modeling of the Ocean and Atmosphere*. Cambridge University Press, 234 pp.
- Bergot, T., 1999: Adaptive observations during FASTEX : A systematic survey of upstream flights. *Q. J. R. Meteorol. Soc.*, **125**, 3271-3298.
- Berliner, L. M., Z.-Q. Lu, and C. Snyder, 1999: Statistical design for adaptive weather observations. *J. Atmos. Sci.*, **56**, 2536-2552.
- Bishop, C. H. and Z. Toth, 1999: Ensemble transformation and adaptive observations. *J. Atmos. Sci.*, **56**, 1748-1765.
- Bishop, C. H., B. J. Etherton, and S. J. Majumdar, 2001: Adaptive sampling with the Ensemble Transform Kalman Filter. Part I: theoretical aspects. *Mon. Weather Rev.*, **129**, 420-436.
- Broquet, G., C. A. Edwards, A. M. Moore, B. S. Powell, M. Veneziani, and J. D. Doyle, 2009: Application of 4D-Variational data assimilation to the California Current System. *Dyn. Atmos. Oceans*, in press.
- Castelao, R. M., O. Schofield, S. Glenn, R. J. Chant, and J. Kohut, 2008a: Cross-shelf transport of fresh water on the New Jersey Shelf. *J. Geophys. Res.*, **113**, C07017.
- Castelao, R. M., S. Glenn, O. Schofield, R. J. Chant, J. Wilkin, and J. Kohut, 2008b: Seasonal evolution of hydrographic fields in the central Middle Atlantic Bight from glider observations. *Geophys. Res. Lett.*, **35**, L03617, doi:10.1029/2007GL032335.

Chant, R. J., S. M. Glenn, E. Hunter, J. Kohut, R. F. Chen, R. W. Houghton, J. Bosch, and O. Schofield, 2008a: Bulge formation of a buoyant river flow. *J. Geophys. Res.*, **113**, C01017, doi:10.1029/2007JC004100.

Chant, R. J., J. Wilkin, W. Zhang, B.-J. Choi, E. Hunter, R. Castelao, S. M. Glenn, J. Jurisa, O. Schofield, R. Houghton, J. Kohut, T. K. Frazer, and M. A. Moline, 2008b: Dispersal of the Hudson River Plume in the New York Bight: synthesis of observational and numerical studies during LaTTE. *Oceanography*, **21**, 148-161.

Chapman, D. C., 1985: Numerical treatment of cross-shelf open boundaries in a barotropic ocean model. *J. Phys. Oceanogr.*, **15**, 1060-1075.

Choi, B.-J. and J. L. Wilkin, 2007: The effect of wind on the dispersal of the Hudson River plume. *J. Phys. Oceanogr.*, **37**, 1878-1897.

Di Lorenzo, E., A. M. Moore, H. G. Arango, B. D. Cornuelle, A. J. Miller, B. Powell, B. S. Chua, and A. Bennett, 2007: Weak and strong constraint data assimilation in the inverse Regional Ocean Modeling System (ROMS): development and application for a baroclinic coastal upwelling system. *Ocean Model.*, **16**, 160-187.

Egbert, G. D. and S. Y. Erofeeva, 2002: Efficient inverse modeling of barotropic ocean tides. *J. Atmos. Oceanic Technol.*, **19**, 183-204.

Fairall, C. W., E. F. Bradley, J. E. Hare, A. A. Grachev, and J. Edson, 2003: Bulk Parameterization of Air–Sea Fluxes: Updates and Verification for the COARE Algorithm. *J. Clim.*, **16**, 571-591.

Flather, R. A., 1976: A tidal model of the northwest European continental shelf. *Mem. Soc. Roy. Sci. Liege, Ser. 6*, **10**, 141-164.

Frolov, S., A. Baptista, and M. Wilkin, 2008: Optimizing fixed observational assets in a coastal observatory. *Cont. Shelf Res.*, **28**, 2644-2658.

Glenn, S. M., J. F. Grassle, and C. J. von Alt, 2000: A well sampled ocean: the LEO approach. *Oceanus*, **42**, 28-30.

Hackert, E. C., R. N. Miller, and A. J. Busalacchi, 1998: An optimized design for a moored instrument array in the tropical Atlantic Ocean. *J. Geophys. Res.*, **103**, 7491-7509.

Harris, C. K., B. Butman, and P. Traykovski, 2003: Winter-time circulation and sediment transport in the Hudson Shelf Valley. *Cont. Shelf Res.*, **23**, 801-820.

Johnson, D. R., J. Miller, and O. Schofield, 2003: Dynamics and optics of the Hudson River outflow plume. *J. Geophys. Res.*, **108**, 3323, doi:10.1029/2002JC001485.

- Kaiser, M. J. and A. G. Pulsipher, 2004: The potential value of improved ocean observation systems in the Gulf of Mexico. *Mar. Policy*, **28**, 469-489.
- Köhl, A. and D. Stammer, 2004: Optimal observations for variational data assimilation. *J. Phys. Oceanogr.*, **34**, 529-542.
- Kohut, J. T., H. J. Roarty, and S. M. Glenn, 2006: Characterizing Observed Environmental Variability with HF Doppler Radar Surface Current Mappers and Acoustic Doppler Current Profilers: Environmental Variability in the Coastal Ocean. *IEEE J. Oceanic Eng.*, **31**, 876-884.
- Kurapov, A. L., G. D. Egbert, J. S. Allen, and R. N. Miller, 2009: Representer-based analyses in the coastal upwelling system. *Dyn. Atmos. Oceans*, in press.
- Langland, R. H., 2005: Issues in targeted observations. *Q. J. R. Meteorol. Soc.*, **131**, 3409-3425.
- Langland, R. H. and N. L. Baker, 2004: Estimation of observation impact using the NRL atmospheric variational data assimilation adjoint system. *Tellus A*, **56**, 189-201.
- Lentz, S. J., 2008: Observations and a model of the mean circulation over the Middle Atlantic Bight continental shelf. *J. Phys. Oceanogr.*, 1203-1221.
- Leutbecher, M., 2003: A reduced rank estimate of forecast error variance changes due to intermittent modification of the observing network. *J. Atmos. Sci.*, **60**, 729-742.
- Manning, J. P., L. Y. Oey, D. Packer, J. Vitaliano, T. W. Finneran, K. W. You, and S. Fromm, 1994: Observations of bottom currents and estimates of resuspended sediment transport at the New York Bight 12-mile dumpsite. *J. Geophys. Res.*, **99**, 10,221-10,239.
- Mayer, D. A., G. C. Han, and D. V. Hansen, 1982: Circulation in the Hudson Shelf Valley: MESA physical oceanographic studies in New York Bight, 1. *J. Geophys. Res.*, **87**, 9563-9578.
- McIntosh, P. C., 1987: Systematic design of observational array. *J. Phys. Oceanogr.*, **17**, 885-902.
- Mesinger, F., G. DiMego, E. Kalnay, K. Mitchell, P. C. Shafran, W. Ebisuzaki, D. Jovian, J. Woollen, E. Rogers, E. H. Berbery, M. B. Ek, Y. Fan, R. Grumbine, W. Higgins, H. Li, Y. Lin, G. Manikin, D. Parrish, and W. Shi, 2006: North American Regional Reanalysis. *Bull. Am. Meteorol. Soc.*, **87**, 343-360.
- Moore, A. M., H. G. Arango, E. Di Lorenzo, A. J. Miller, and B. D. Cornuelle, 2008: An adjoint sensitivity analysis of the Southern California Current circulation and ecosystem. Part I: The physical circulation. *J. Phys. Oceanogr.*, in press.

- Moore, A. M., H. G. Arango, E. Di Lorenzo, B. D. Cornuelle, A. J. Miller, and D. J. Neilson, 2004: A Comprehensive Ocean Prediction and Analysis System Based on the Tangent Linear and Adjoint of a Regional Ocean Model. *Ocean Model.*, **7**, 227-258.
- Mukai, A. Y., J. J. Westerink, R. A. Luetlich, and D. Mark, 2002: Eastcoast 2001, A tidal constituent database for the western North Atlantic, Gulf of Mexico and Caribbean Sea, Tech. Rep. ERDC/CHL TR-02-24, 196 pp.
- Nelson, T. A., P. E. Gadd, and T. L. Clarke, 1978: Wind-induced current flow in the upper Hudson Shelf Valley. *J. Geophys. Res.*, **83**, 6073-6082.
- Oke, P. R. and A. Schiller, 2007: A model-based assessment and design of a tropical Indian Ocean mooring Array. *J. Clim.*, **20**, 3269-3283.
- Orlanski, I., 1976: A simple boundary condition for unbounded hyperbolic flows. *J. Comput. Phys.*, **21**, 251-269.
- Palmer, T. N., R. Gelaro, J. Barkmeijer, and R. Buizza, 1998: Singular Vectors, Metrics, and Adaptive Observations. *J. Atmos. Sci.*, **55**, 633-653.
- Powell, B. S. and A. M. Moore, 2008: Estimating the 4DVAR analysis error of GODAE products. *Ocean Dynam.*, in press.
- Powell, B. S., A. M. Moore, H. Arango, E. Di Lorenzo, R. Milliff, and R. R. Leben, 2008a: Near real-time assimilation and prediction in the Intra-Americas Sea with the Regional Ocean Modeling System (ROMS). *Dynamics of Atmospheres and Oceans*, In press.
- Powell, B. S., H. G. Arango, A. M. Moore, E. Di Lorenzo, R. F. Milliff, and D. Foley, 2008b: 4DVAR data assimilation in the Intra-Americas Sea with the Regional Ocean Modeling System (ROMS). *Ocean Model.*, **25**, 173-188.
- Rabier, F., P. Gauthier, C. Cardinali, R. Langland, M. Tsyrlnikov, A. Lorenc, P. Steinle, R. Gelaro, and K. Koizumi, 2008: An update on THORPEX-related research in data assimilation and observing strategies. *Nonlin. Processes Geophys.*, **15**, 81-94.
- Sakov, P. and P. R. Oke, 2008: Objective array design: application to the tropical Indian Ocean. *J. Atmos. Oceanic Technol.*, **25**, 794-807.
- Schofield, O., R. Arnone, P. Bissett, T. D. Dickey, C. Davis, Z. Finkel, M. Oliver, and M. A. Moline, 2004: Watercolors in the coastal zone: what can we see? *Oceanography*, **17**, 30-37.
- Schofield, O., J. Kohut, D. Aragon, L. Creed, J. Graver, C. Haldeman, J. Kerfoot, H. Roarty, C. Jones, D. Webb, and S. M. Glenn, 2007: Slocum gliders: robust and ready. *J. Field Robot.*, **24**, 1-14.

- Shulman, I., D. J. McGillicuddy, M. A. Moline, S. H. D. Haddock, J. C. Kindle, D. Nechaev, and M. W. Phelps, 2005: Bioluminescence intensity modeling and sampling strategy optimization. *J. Atmos. Oceanic Technol.*, **22**, 1267-1281.
- Tilburg, C. E. and R. W. Garvine, 2003: Three-dimensional flow in a coastal upwelling zone: Convergence and divergence on the New Jersey Shelf. *J. Phys. Oceanogr.*, **33**, 2113-2115.
- Umlauf, L. and H. Burchard, 2003: A generic length-scale equation for geophysical turbulence models. *J. Mar. Res.*, **61**, 235-265.
- van Leeuwen, P. J. and G. Evensen, 1996: Data assimilation and inverse methods in terms of a probabilistic formulation. *Mon. Weather Rev.*, **124**, 2898-2913.
- Warner, J. C., C. R. Sherwood, H. G. Arango, R. P. Signell, and B. Butman, 2005: Performance of four turbulence closure models implemented using a generic length scale method. *Ocean Model.*, **8**, 81-113.
- Wilkin, J. L., H. G. Arango, D. B. Haidvogel, C. S. Lichtenwalner, S. M. Glenn, and K. S. Hedström, 2005: A Regional Ocean Modeling System for the Long-term Ecosystem Observatory. *J. Geophys. Res.*, **110**, doi:10.1029/2003JC002218.
- Wong, K. C., 1999: The wind driven currents on the Middle Atlantic Bight inner shelf. *Cont. Shelf Res.*, **19**, 757-773.
- Wu, C.-C., J.-H. Chen, P.-H. Lin, and K.-H. Chou, 2007: Targeted observations of tropical cyclone movement based on the Adjoint-Derived Sensitivity Steering Vector. *J. Atmos. Sci.*, **64**, 2611-2626.
- Yankovsky, A. E., 2003: The cold-water pathway during an upwelling event on the New Jersey shelf. *J. Phys. Oceanogr.*, **33**, 1954-1966.
- Yankovsky, A. E. and R. W. Garvine, 1998: Subinertial Dynamics on the Inner New Jersey Shelf during the Upwelling Season. *J. Phys. Oceanogr.*, **28**, 2444-2458.
- Yankovsky, A. E., R. W. Garvine, and A. Munchow, 2000: Mesoscale Currents on the Inner New Jersey Shelf Driven by the Interaction of Buoyancy and Wind Forcing. *J. Phys. Oceanogr.*, **30**, 2214-2230.
- Zhang, W. G., J. L. Wilkin, and R. J. Chant, 2009a: Modeling the pathways and mean dynamics of river plume dispersal in New York Bight. *J. Phys. Oceanogr.*, **39**, 1167-1183.
- Zhang, W. G., J. L. Wilkin, and H. G. Arango, 2009b: Towards an integrated observation and modeling system in the New York Bight using variational methods, Part I: 4DVAR Data Assimilation. *Ocean Model.*, sub judice.

Zhang, W. G., J. L. Wilkin, J. C. Levin, and H. G. Arango, 2009c: An Adjoint Sensitivity Study of Buoyancy- and Wind-driven Circulation on the New Jersey Inner Shelf. *J. Phys. Oceanogr.*, **39**, 1652-1668.

Figure Captions

Figure 1. The model domain (black frame) and bathymetry of the New York Bight in grayscale. The short straight line across the Hudson Shelf Valley indicates the cross-section used to compute salt transport within the valley; the dash line is the so-called *Endurance Line* glider track regularly sampled by RU-COOL; the long straight black line is the hypothetical glider track; and the triangle indicates the location of the hypothetical mooring.

Figure 2. Surface salinity (top) and surface salinity representer (bottom) at different times in 2006. The triangles in the last column indicate the point of interest at which J is defined; the straight lines passing through that point in the last panel indicate the cross-sections plotted in Figure 3; and gray dash lines are 20, 40 and 60 m isobaths.

Figure 3. Cross-sections of the salinity representer field at 2006-09-18 00:00 UTC, the time when J is defined. The positions of the cross-sections are depicted in Figure 2.

Figure 4. Seasonal averages of salinity (in color) and current (arrows) at 20 m depth. Gray lines are 20, 40, 60 m isobaths and the thick black lines indicate the cross-section of the Hudson Shelf Valley used to compute the salt flux.

Figure 5. Time series of the modeled subsurface (below 10 m) along-valley salt flux within the Hudson Shelf Valley during 2006. The thin gray line is the daily-averaged time series and the thick black line is 24-day low-pass filtered. Positive is shoreward.

Figure 6. Flows of the representer computation and corresponding twin experiment. J_t is the “true” salt flux from the control run; $\partial J / \partial \phi$ indicates corresponding adjoint forcing; \mathbf{B} is the background error covariance; triangle indicates the time of the presented

combination of representers (2 days before the time interval over which J_t is defined); obs. indicates the observation window; J_b is the background salt flux from the perturbed simulation; DA indicates the data assimilation window; J_a is the salt flux forecast given by the models after data assimilation.

Figure 7. Average salinity correlation field at 20 m for different seasons. Gray lines are 20, 40 and 60 m isobaths and the thick black lines indicate the Hudson Shelf Valley cross-section where J is defined. Triangles indicate the optimal glider track and circles the traditional.

Figure 8. Skills of the two twin experiment systems in terms of predicting salt flux within the Hudson Shelf Valley for (a) summer-fall and (b) winter-spring seasons. Vertical bars are 95% confidence interval.

Figure 9. Representer-based influence of observations from a glider section (black straight lines in top row) and a fixed mooring (white triangle in bottom row) at different times. The influence is measured by the gain function defined in the text. The observational period is day 0 to day 3. Days 3 to 6 represent the influence of observations on the forecast computed by the model.

Figure 10. Vertical cross-sections of the representer-based influence, at different times, of glider and mooring observations along the glider track in Figure 9. The white lines in the second column indicate the mooring location. The observational period is day 0 to day 3. Days 3 to 6 represent the influence of observations on the forecast computed by the model.

Figure 11. Representer-based influence of a glider section (white lines) at different times in wind-driven coast upwelling (top row) and down-welling (bottom row) regimes.

Figure 12. Contours of representer-based influence of a glider section (black straight lines) at day 3 (top row) and day 6 (bottom row) in systems with different durations of the data assimilation window. The contour lines are 0.01, 0.1, 0.5 °C. The observations were taken at day 3.

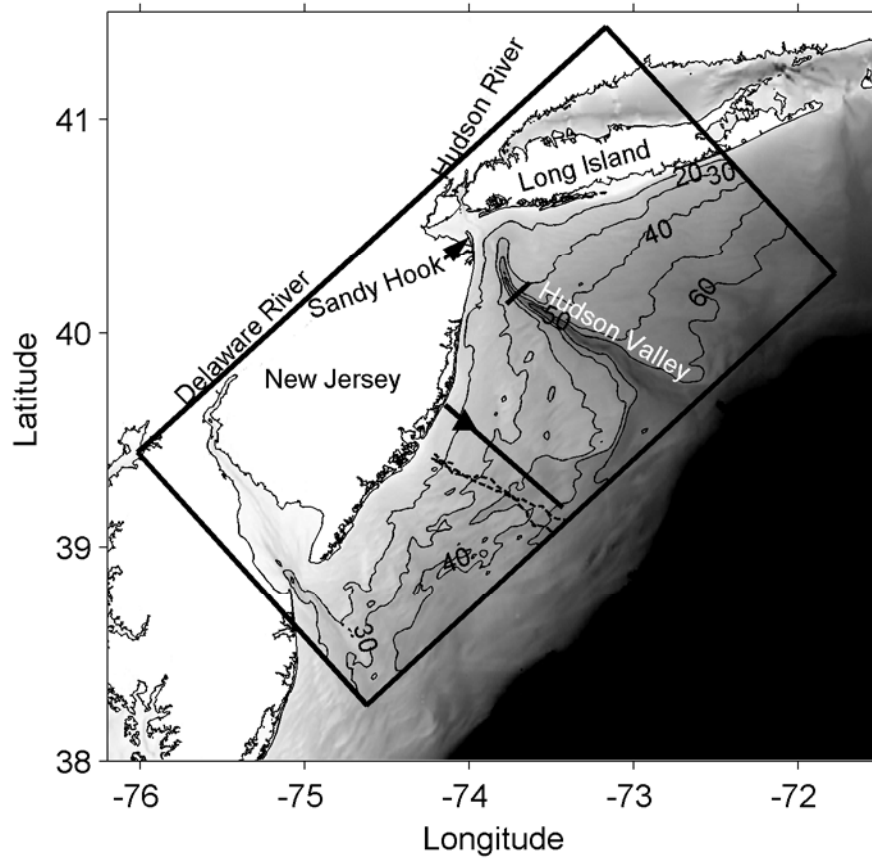


Figure 1. The model domain (black frame) and bathymetry of the New York Bight in grayscale. The short straight line across the Hudson Shelf Valley indicates the cross-section used to compute salt transport within the valley; the dash line is the so-called *Endurance Line* glider track regularly sampled by RU-COOL; the long straight black line is the hypothetical glider track; and the triangle indicates the location of the hypothetical mooring.

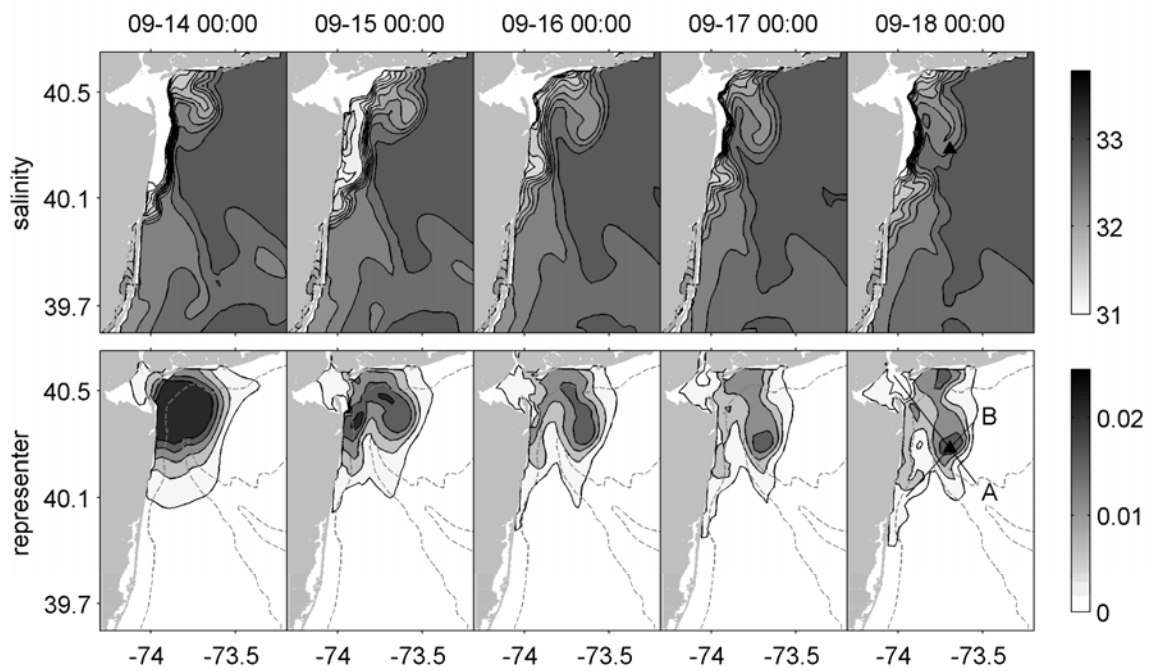


Figure 2. Surface salinity (top) and surface salinity representer (bottom) at different times in 2006. The triangles in the last column indicate the point of interest at which J is defined; the straight lines passing through that point in the last panel indicate the cross-sections plotted in Figure 3; and gray dash lines are 20, 40 and 60 m isobaths.

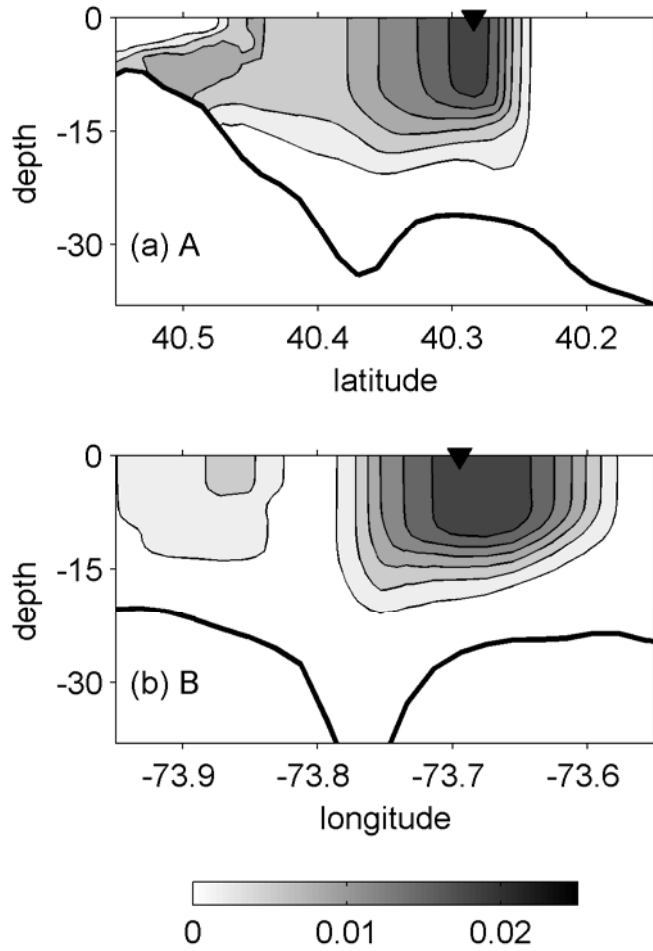


Figure 3. Cross-sections of the salinity representer field at 2006-09-18 00:00 UTC, the time when J is defined. The positions of the cross-sections are depicted in Figure 2.

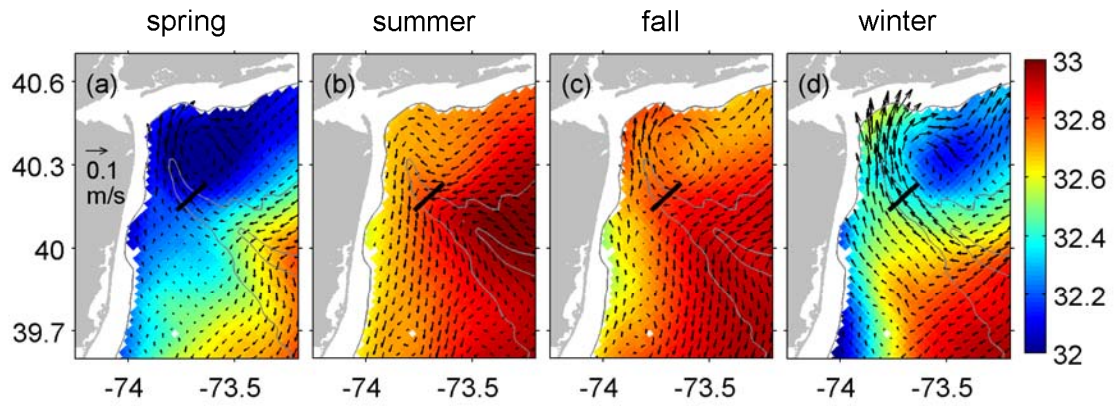


Figure 4. Seasonal averages of salinity (in color) and current (arrows) at 20 m depth. Gray lines are 20, 40, 60 m isobaths and the thick black lines indicate the cross-section of the Hudson Shelf Valley used to compute the salt flux.

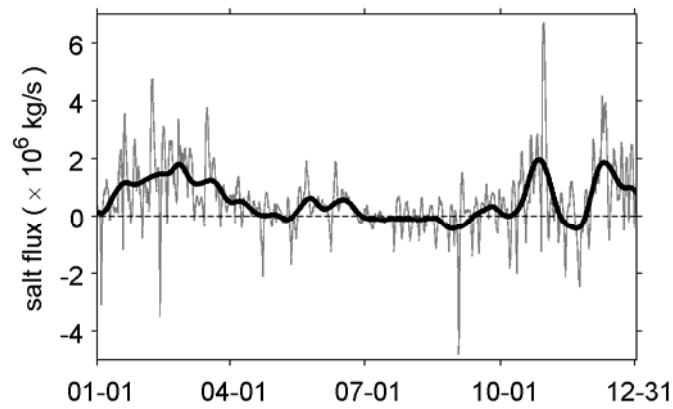


Figure 5. Time series of the modeled subsurface (below 10 m) along-valley salt flux within the Hudson Shelf Valley during 2006. The thin gray line is the daily-averaged time series and the thick black line is 24-day low-pass filtered. Positive is shoreward.

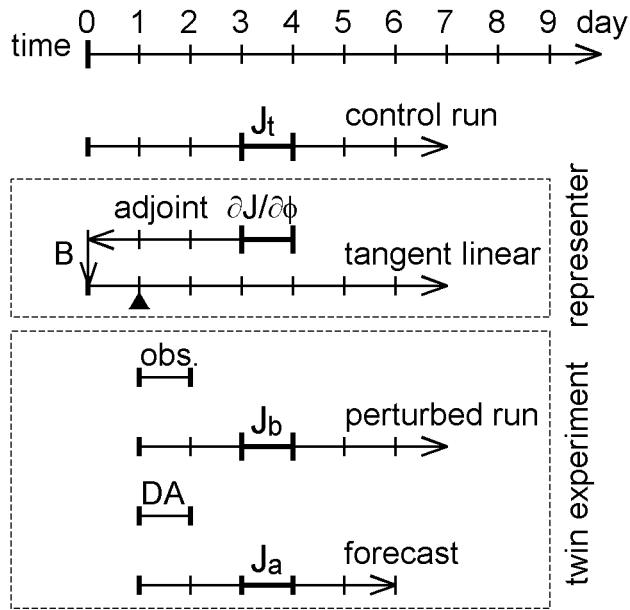


Figure 6. Flows of the representer computation and corresponding twin experiment. J_t is the “true” salt flux from the control run; $\partial J/\partial \phi$ indicates corresponding adjoint forcing; \mathbf{B} is the background error covariance; triangle indicates the time of the presented combination of representers (2 days before the time interval over which J_t is defined); obs. indicates the observation window; J_b is the background salt flux from the perturbed simulation; DA indicates the data assimilation window; J_a is the salt flux forecast given by the models after data assimilation.

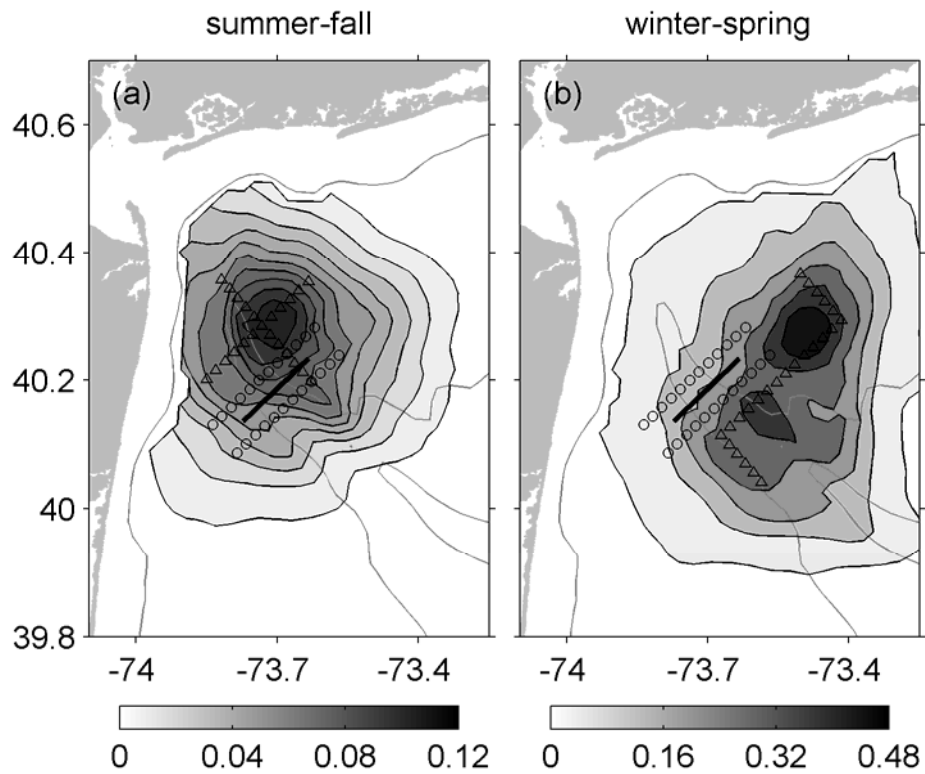


Figure 7. Average salinity correlation field at 20 m for different seasons. Gray lines are 20, 40 and 60 m isobaths and the thick black lines indicate the Hudson Shelf Valley cross-section where J is defined. Triangles indicate the optimal glider track and circles the traditional.

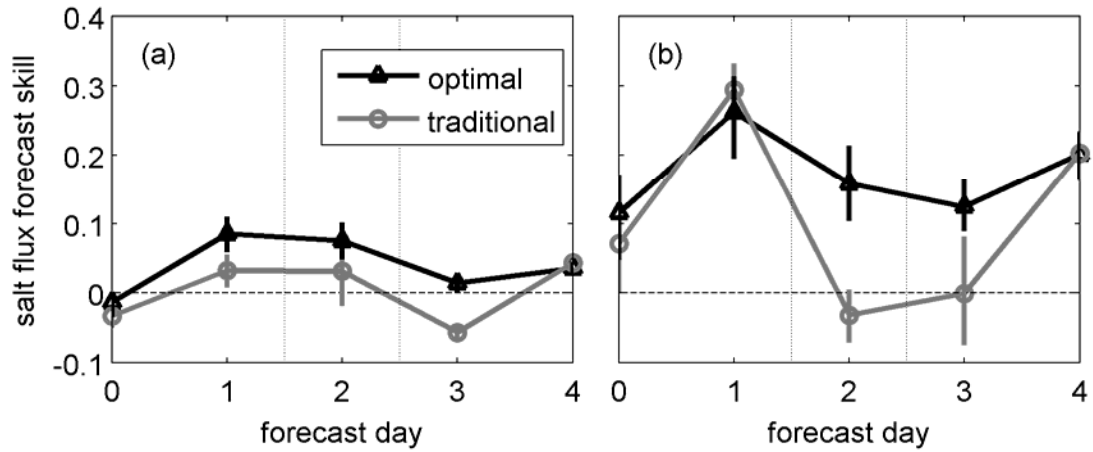


Figure 8. Skills of the two twin experiment systems in terms of predicting salt flux within the Hudson Shelf Valley for (a) summer-fall and (b) winter-spring seasons. Vertical bars are 95% confidence interval.

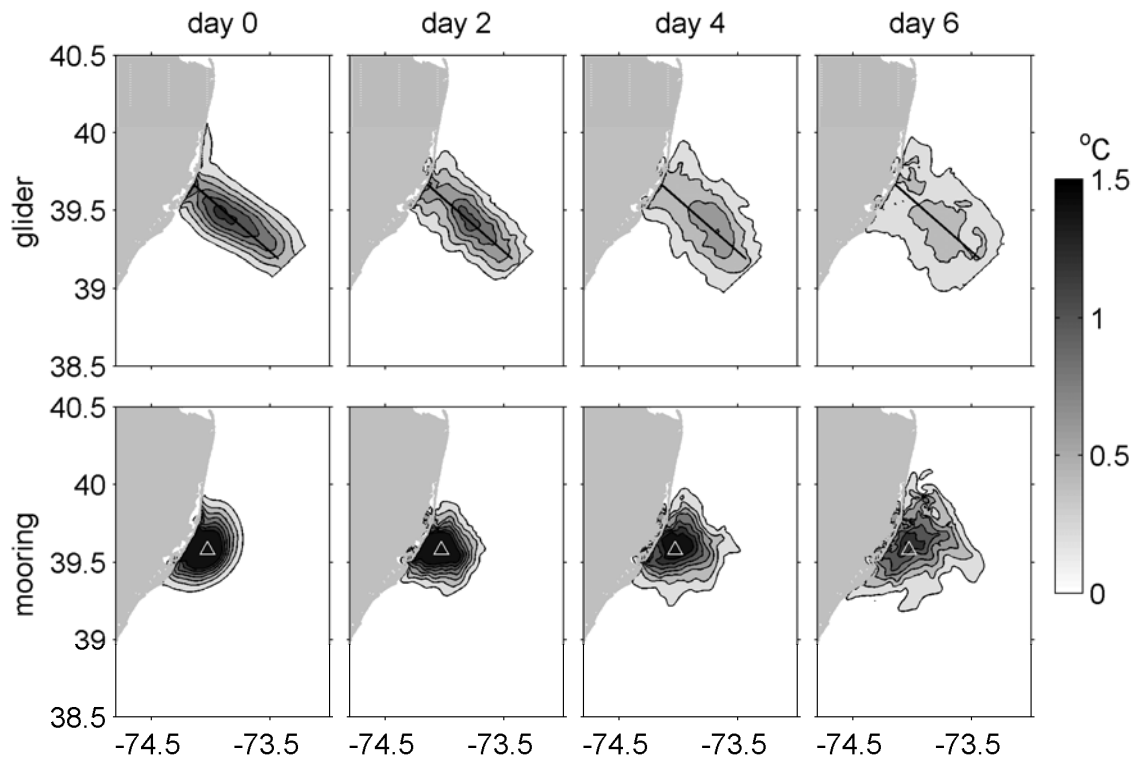


Figure 9. Representer-based influence of observations from a glider section (black straight lines in top row) and a fixed mooring (white triangle in bottom row) at different times. The influence is measured by the gain function defined in the text. The observational period is day 0 to day 3. Days 3 to 6 represent the influence of observations on the forecast computed by the model.

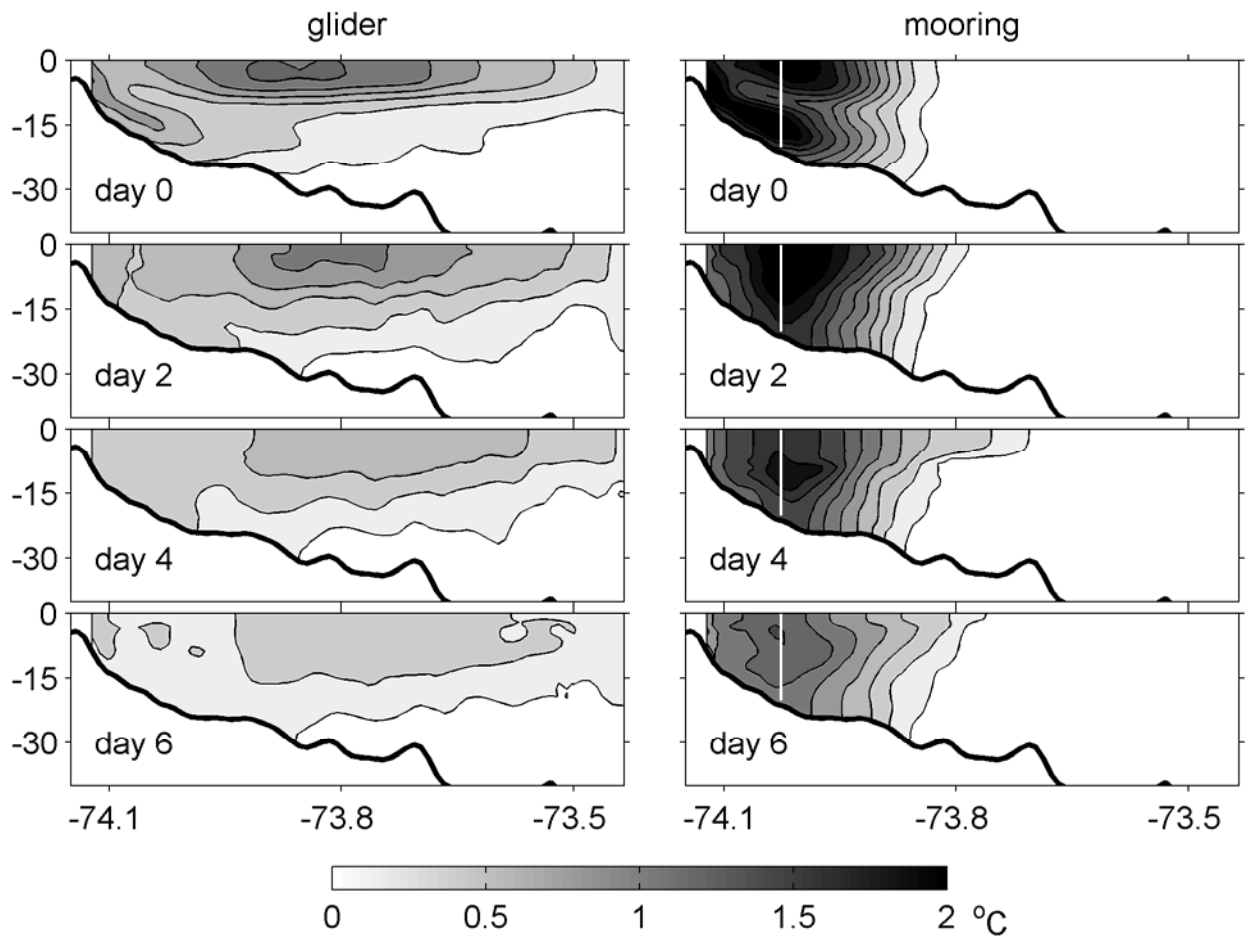


Figure 10. Vertical cross-sections of the representer-based influence, at different times, of glider and mooring observations along the glider track in Figure 9. The white lines in the second column indicate the mooring location. The observational period is day 0 to day 3. Days 3 to 6 represent the influence of observations on the forecast computed by the model.

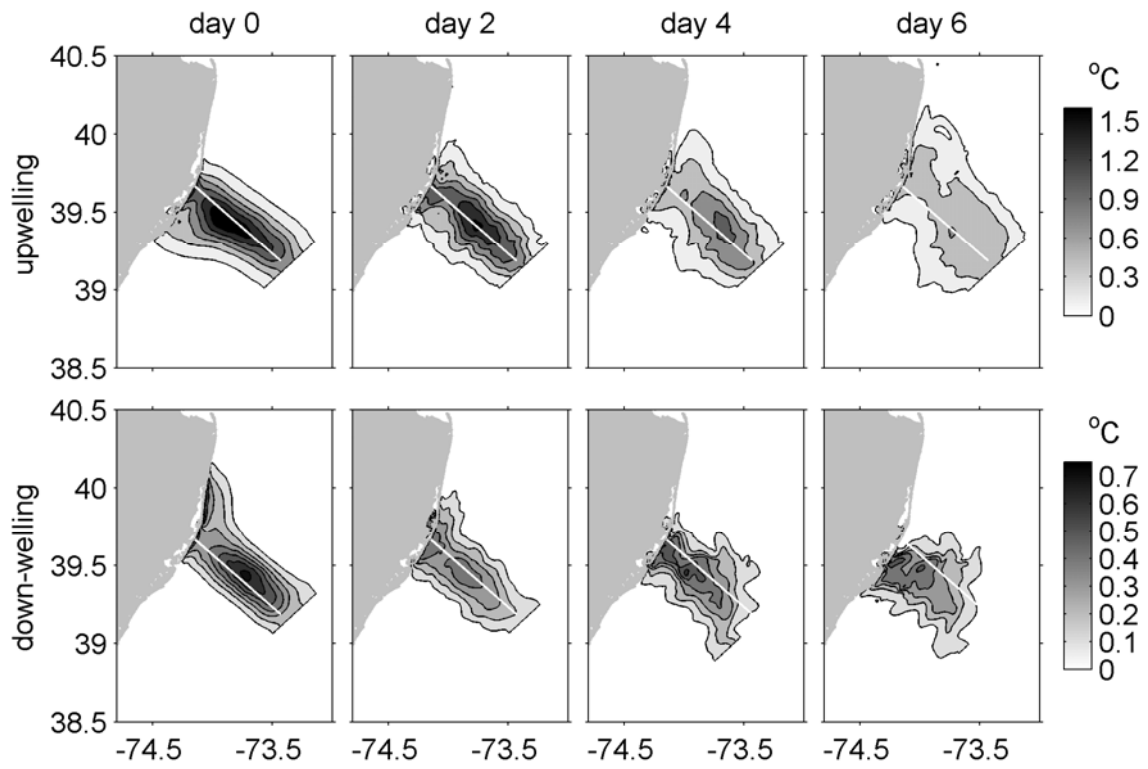


Figure 11. Representer-based influence of a glider section (white lines) at different times in wind-driven coast upwelling (top row) and down-welling (bottom row) regimes.

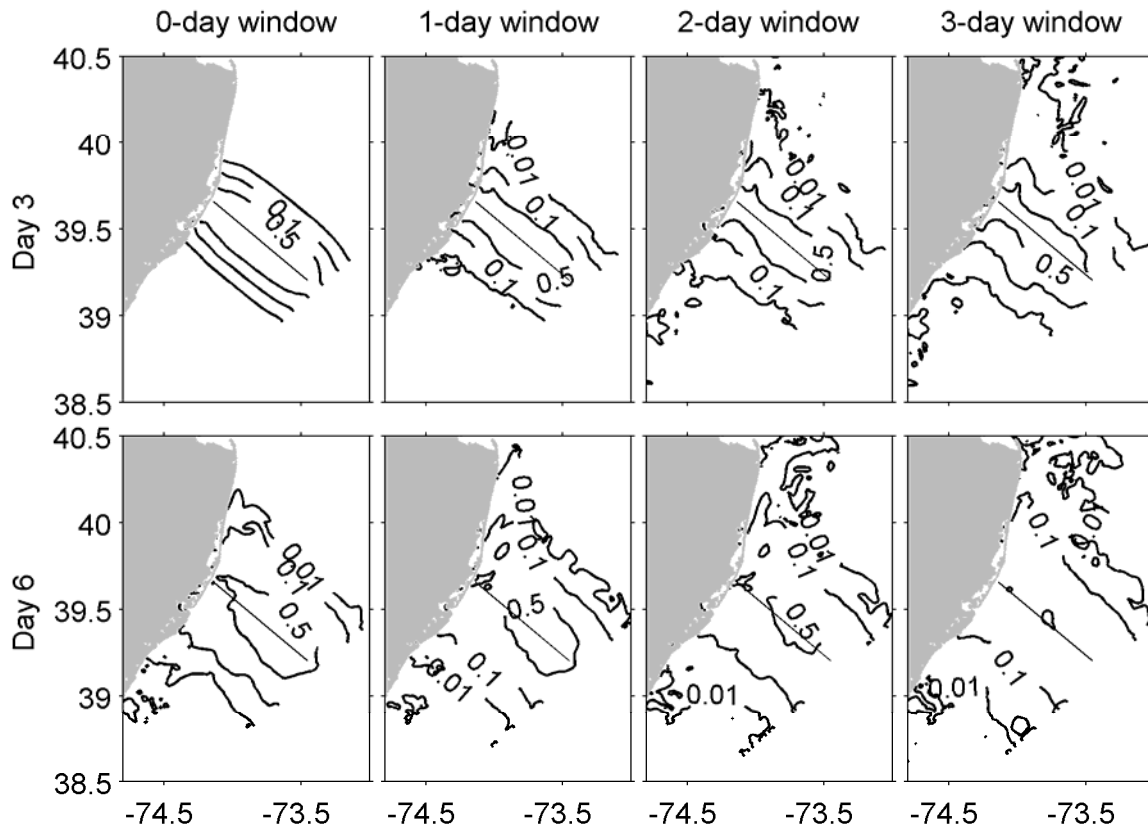


Figure 12. Contours of representer-based influence of a glider section (black straight lines) at day 3 (top row) and day 6 (bottom row) in systems with different durations of the data assimilation window. The contour lines are 0.01, 0.1, 0.5 °C. The observations were taken at day 3.